

1 In Situ Tracking of Colloidally Stable and Ordered Assemblies of 2 Gold Nanorods

3 Dorota Grzelak, Piotr Szustakiewicz, Christopher Tollan, Sanoj Raj, Petr Král,* Wiktor Lewandowski,*
4 and Luis M. Liz-Marzán*



Cite This: <https://dx.doi.org/10.1021/jacs.0c06446>



Read Online

ACCESS |



Metrics & More

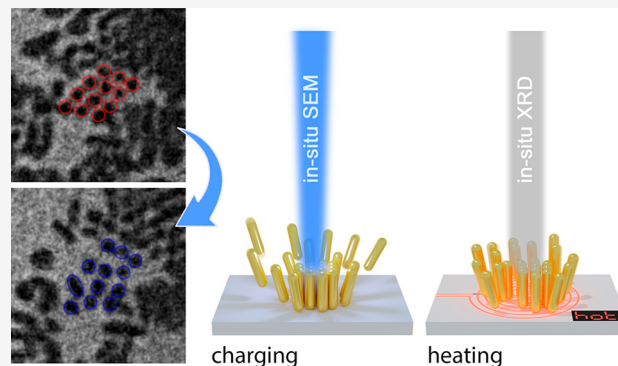


Article Recommendations



Supporting Information

5 **ABSTRACT:** Solution-phase self-assembly of anisotropic nano-
6 particles into complex 2D and 3D assemblies is one of the most
7 promising strategies toward obtaining nanoparticle-based materials
8 and devices with unique optical properties at the macroscale.
9 However, controlling this process with single-particle precision is
10 highly demanding, mostly due to insufficient understanding of the
11 self-assembly process at the nanoscale. We report the use of in situ
12 environmental scanning transmission electron microscopy (Wet-
13 STEM), combined with UV/vis spectroscopy, small-angle X-ray
14 diffraction (SAXRD) and multiscale modeling, to draw a detailed
15 picture of the dynamics of vertically aligned assemblies of gold
16 nanorods. Detailed understanding of the self-assembly/disassembly
17 mechanisms is obtained from real-time observations, which provide
18 direct evidence of the colloidal stability of side-to-side nanorod
19 clusters. Structural details and the forces governing the disassembly process are revealed with single particle resolution as well as in
20 bulk samples, by combined experimental and theoretical modeling. In particular, this study provides unique information on the
21 evolution of the orientational order of nanorods within side-to-side 2D assemblies and shows that both electrostatic (at the
22 nanoscale) and thermal (in bulk) stimuli can be used to drive the process. These results not only give insight into the interactions
23 between nanorods and the stability of their assemblies, thereby assisting the design of ordered, anisotropic nanomaterials but also
24 broaden the available toolbox for in situ tracking of nanoparticle behavior at the single particle level.



25 ■ INTRODUCTION

26 Ordered assemblies of gold nanorods (AuNRs) offer
27 extraordinary properties with potential applications in various
28 technologies, such as chemical and biological sensing,^{1–3} in
29 vivo medical studies,^{4,5} catalysis,^{6–8} data storage,⁹ and
30 optoelectronics.¹⁰ The main reason for such a broad
31 applicability is that these materials translate the anisotropic
32 functionality of single particles into micro/macro-(ensemble)
33 scale anisotropy. However, building ordered structures out of
34 AuNRs still poses a significant challenge, due to our limited
35 knowledge regarding the dynamics of the self-assembly
36 process. This limitation largely results from our current
37 inability, either to monitor in situ the behavior of thousands
38 of nanoparticles at the macro-scale (e.g., via UV/vis spectro-
39 scopy)¹¹ or to take ex situ snapshots at the single particle level
40 from static structures (e.g. via electron microscopy).¹²
41 Development of methods for in situ monitoring the behavior
42 of single AuNRs in solution should bring us closer to a
43 complete understanding of the self-assembly mechanism and
44 achieving full control over this process.

45 In situ electron microscopy (EM) observation of nano-
46 particle dispersions under dynamic conditions has recently

47 allowed for real-time visualization of chemical and physical
48 events at the single nanoparticle level. Some remarkable
49 examples include the observation of how spherical¹³ and
50 anisotropic nanoparticles grow,¹⁴ nanoparticle surface oxida-
51 tion,¹⁵ or dehydrogenation.¹⁶ More recently, in situ EM has
52 also been used to investigate self-assembly processes. It
53 allowed, e.g., to analyze the influence and contribution of
54 hydrophobic,¹⁷ van der Waals,¹⁸ and electrostatic forces¹⁹ on
55 the kinetics and the outcome of the self-assembly process.
56 However, most of the reported in situ investigations are
57 concerned with the assembly of spherical nanoparticles, and
58 the acquired knowledge cannot be directly translated to the
59 self-assembly principles of anisotropic nanoparticles, since the
60 latter exhibit anisotropic interactions and yield complex 3D

Received: June 14, 2020

Published: September 29, 2020

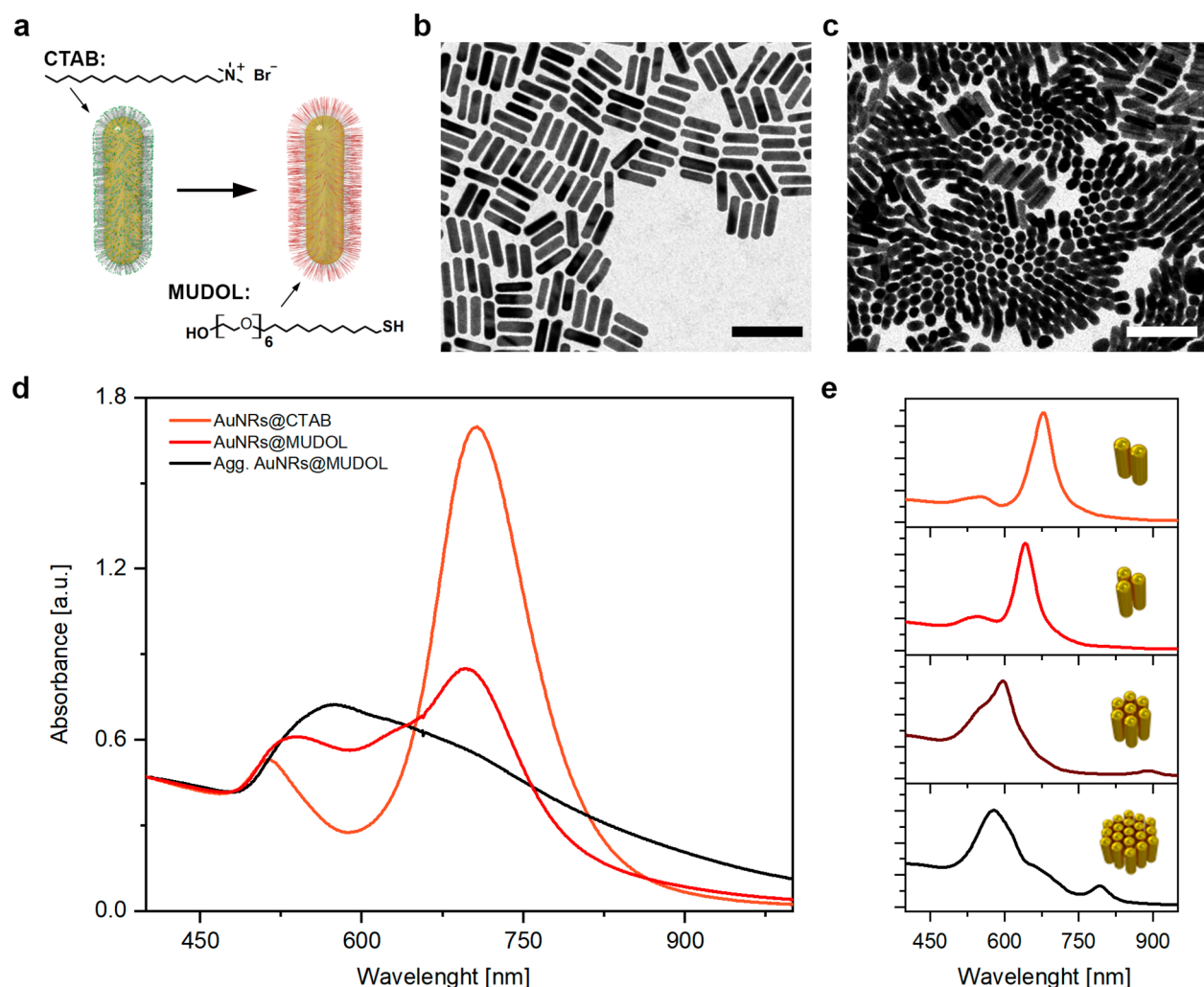


Figure 1. Synthesis and characterization of AuNRs. (a) Scheme of the ligand exchange reaction performed on AuNR@CTAB, to obtain AuNR@MUDOL. (b) Representative TEM image of horizontally deposited AuNR@CTAB assemblies. (c) Representative TEM image of vertical AuNR@MUDOL assemblies. (d) UV/vis spectra of AuNR@CTAB, AuNR@MUDOL directly after ligand exchange and 2 h after completing the ligand exchange reaction; spectra were normalized at 400 nm. (e) FDTD-modeled UV/vis spectra for AuNR assemblies comprising two, three, seven, and 19 parallel nanorods.

61 architectures with orientational order, as well as potential
62 polymorphic behavior.^{20–22}

63 Recent reports have focused on in situ imaging of the self-
64 assembly of anisotropic nanoparticles, providing insight into
65 the behavior of nanocubes,¹⁷ branched nanooctapods,²³ and
66 nanoprisms.^{24,25} In the case of NRs two reports on in situ
67 imaging should be highlighted. Alivisatos et al.²⁶ analyzed
68 trajectories of hexadecyltrimethylammonium bromide
69 (CTAB)-coated AuNRs, revealing long-range and highly
70 anisotropic electrostatic repulsion forces that lead to tip-
71 selective nanorod attachment. Mirsaidov et al.²⁷ followed the
72 assembly of cysteamine-coated AuNRs at different concen-
73 trations of linker molecules, leading to the selective formation
74 of either tip-to-tip or side-to-side clusters. These reports
75 confirm that studying anisotropic nanoparticle interactions at
76 the single particle level provides useful information on their
77 self-assembly. However, these reports focus only on the
78 formation of 1D, few-nanoparticle clusters. Of more general
79 interest but also significantly more challenging is the in situ
80 characterization of assembly and disassembly processes within
81 larger, long-range-ordered assemblies of higher dimensionality.
82 An interesting example in this direction has been recently

reported for the case of triangular Au nanoprisms, which 83
revealed new information on the crystallization of such 84
nanoparticles, further confirming the importance of single- 85
particle level observations of the self-assembly of anisotropic 86
nanoparticles.²⁵ This is especially important regarding vertical 87
assemblies of nanorods.^{10,12} Although early in situ EM studies 88
enabled the observation of large, vertical assemblies of AuNRs, 89
the time scale of the experiments did not allow the observation 90
of single particle events or any qualitative and/or quantitative 91
analysis of the behavior in solution.²⁸ 92

In this work, we demonstrate the use of environmental 93
scanning transmission electron microscopy (WetSTEM²⁸) to 94
characterize in situ the dynamics of relatively large, 2D, vertical 95
assemblies of AuNRs in the wet state. We were able to monitor 96
the dynamics of single nanoparticles and track the self- 97
assembly and disassembly pathways, for orientationally ordered 98
AuNR aggregates. By combining results of in situ EM, 99
atomistic modeling and ensemble measurements (small-angle 100
X-ray diffraction and UV/vis spectroscopy), we can describe 101
the colloidal stability of side-to-side organized nanorod clusters 102
in solution, thereby gathering insights into the self-assembly 103
mechanism. Additionally, we observe that AuNRs can preserve 104

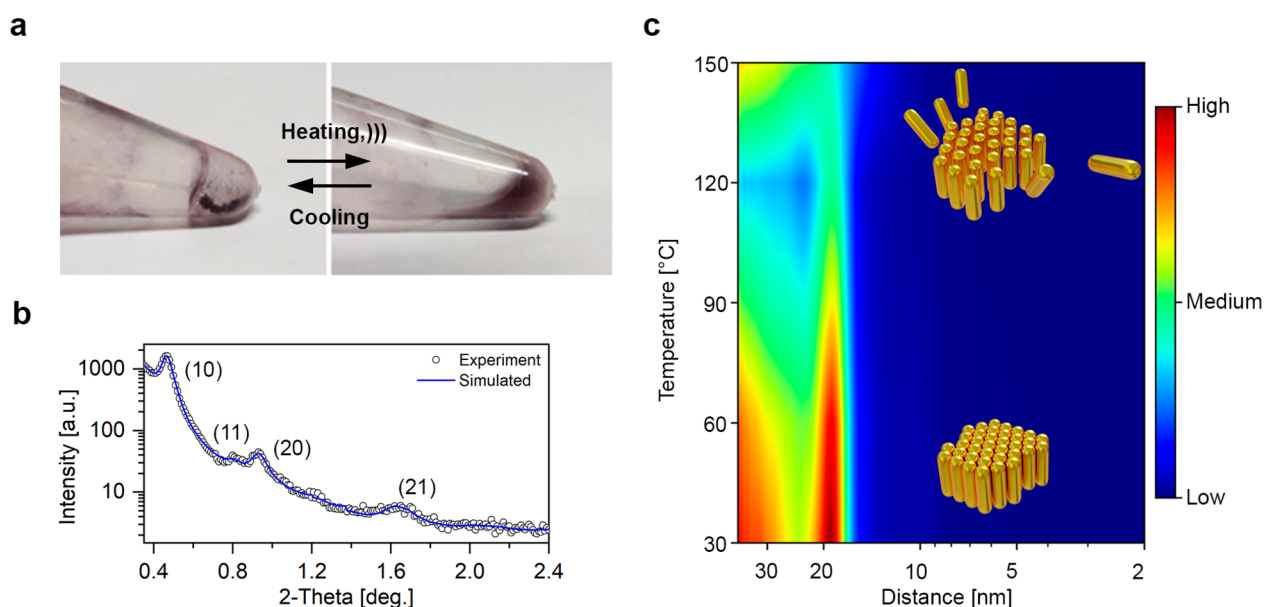


Figure 2. Dynamic self-assembly of AuNR@MUDOL. (a) Photographs of an Eppendorf tube containing precipitated AuNR@MUDOL, 2 h after ligand exchange and the same vial after heating and sonication, evidencing redispersion of AuNR aggregates. (b) 1D SAXRD diffractogram of AuNR@MUDOL, collected at 30 °C. (c) Temperature evolution of SAXRD diffractograms for AuNR@MUDOL aggregates in a 30–150 °C temperature range; two distinct areas can be distinguished: low temperature phase (2D, hexagonal, 30–120 °C) and isotropic phase (120–150 °C).

105 their orientational order during disassembly and confirm
 106 through both experiments and theoretical modeling that both
 107 electrostatic and thermal stimuli can play a major role in the
 108 process.

109 ■ RESULTS AND DISCUSSION

110 **Synthesis and Static Characterization of AuNR@**
 111 **MUDOL Assemblies.** Gold nanorods are arguably the most
 112 widely used nonspherical nanoparticles, due to the relative
 113 simplicity of their synthesis and to their outstanding plasmonic
 114 properties. The AuNRs used in this work were synthesized by
 115 following a seed-mediated method,²⁹ and synthetic details are
 116 given in the **Experimental Section**. As-obtained AuNRs, 52 ×
 117 16 nm (**Supporting Information**, Figure S1), were stabilized by
 118 CTAB (AuNR@CTAB).³⁰ Although some reports have
 119 demonstrated the formation of 3D oriented arrays of
 120 AuNR@CTAB,³¹ the formation and stability of extended
 121 supercrystals is known to be enhanced upon exchanging CTAB
 122 molecules with (1-mercaptopundec-11-yl)hexa(ethylene glycol)
 123 (MUDOL) ligands (**Figure 1a**).^{32,33} AuNR@MUDOL have
 124 lower surface charge and display lower colloidal stability in
 125 aqueous dispersions as compared to AuNR@CTAB, and as a
 126 consequence, stronger side-to-side interactions have been
 127 proposed to lead to parallel aggregation and subsequent
 128 deposition as vertical assemblies (induced by the Marangoni
 129 effect).¹⁰ Under the same experimental conditions, we
 130 confirmed that TEM images of drop-casted AuNR@CTAB
 131 resulted in horizontally oriented AuNR assemblies (**Figure 1b**),
 132 whereas for AuNR@MUDOL, multiple vertically oriented
 133 AuNR domains were evidenced (**Figure 1c**). The measured
 134 center-to-center distance between nanorods within the
 135 observed vertical domains was ~20 nm, which is reasonable
 136 given the diameter of AuNRs (~16 nm) and the thickness of
 137 the organic coating (~2 nm).¹² To further confirm successful
 138 ligand exchange, and to get insight into the colloidal behavior
 139 of Au nanorods, we carried out UV/vis spectroscopy

measurements. AuNR@CTAB exhibit two localized surface
 140 plasmon resonance (LSPR) bands, corresponding to transverse
 141 and longitudinal modes, with maxima at 511 and 707 nm,
 142 respectively, which are characteristic of noninteracting, well-
 143 dispersed particles. After ligand exchange, the AuNR@
 144 MUDOL dispersion exhibits two maxima at 536 and 695
 145 nm, suggesting the formation of colloidal AuNR clusters.³⁴
 146 When the same dispersion was measured 2 h after completing
 147 ligand exchange, we observed a further blue shift and damping
 148 of the longitudinal LSPR band, along with a redshift of the
 149 transverse band, resulting in a single, broad band with a
 150 maximum at 562 nm (**Figure 1d**). To understand the origin of
 151 the observed changes in the plasmonic properties of AuNR@
 152 MUDOL, in terms of their assembly state, we performed
 153 electromagnetic modeling of side-to-side ordered AuNR
 154 clusters. Extinction spectra for AuNRs (with dimensions
 155 corresponding to those used in the experiments) were modeled
 156 using the finite difference time domain (FDTD) method (see
 157 the **Experimental Section** for details).³⁵ We focused on five
 158 different scenarios: a single AuNR and aggregates comprising
 159 two, three, seven, and 19 AuNRs. As shown in **Figure 1e**, the
 160 modeled spectra reveal a gradual blue-shift and broadening of
 161 the LSPR band for a growing number of particles in the cluster.
 162 This is in agreement with our experimental results (**Figure 1d**)
 163 and with previous examples in the literature,³⁶ so we can
 164 conclude that the observed changes in absorbance spectra for
 165 AuNR@MUDOL result from the gradual aggregation of
 166 nanorods into parallel clusters, in the aqueous phase. The
 167 above-discussed results from bulk characterization of AuNR@
 168 MUDOL dispersions confirm their tendency to form side-to-
 169 side assemblies in solution, which would result in the
 170 formation of vertically aligned assemblies on a substrate.
 171 Although the latter is known from the literature,^{10,12} the
 172 reversibility of such an aggregation process has not been
 173 reported. 174

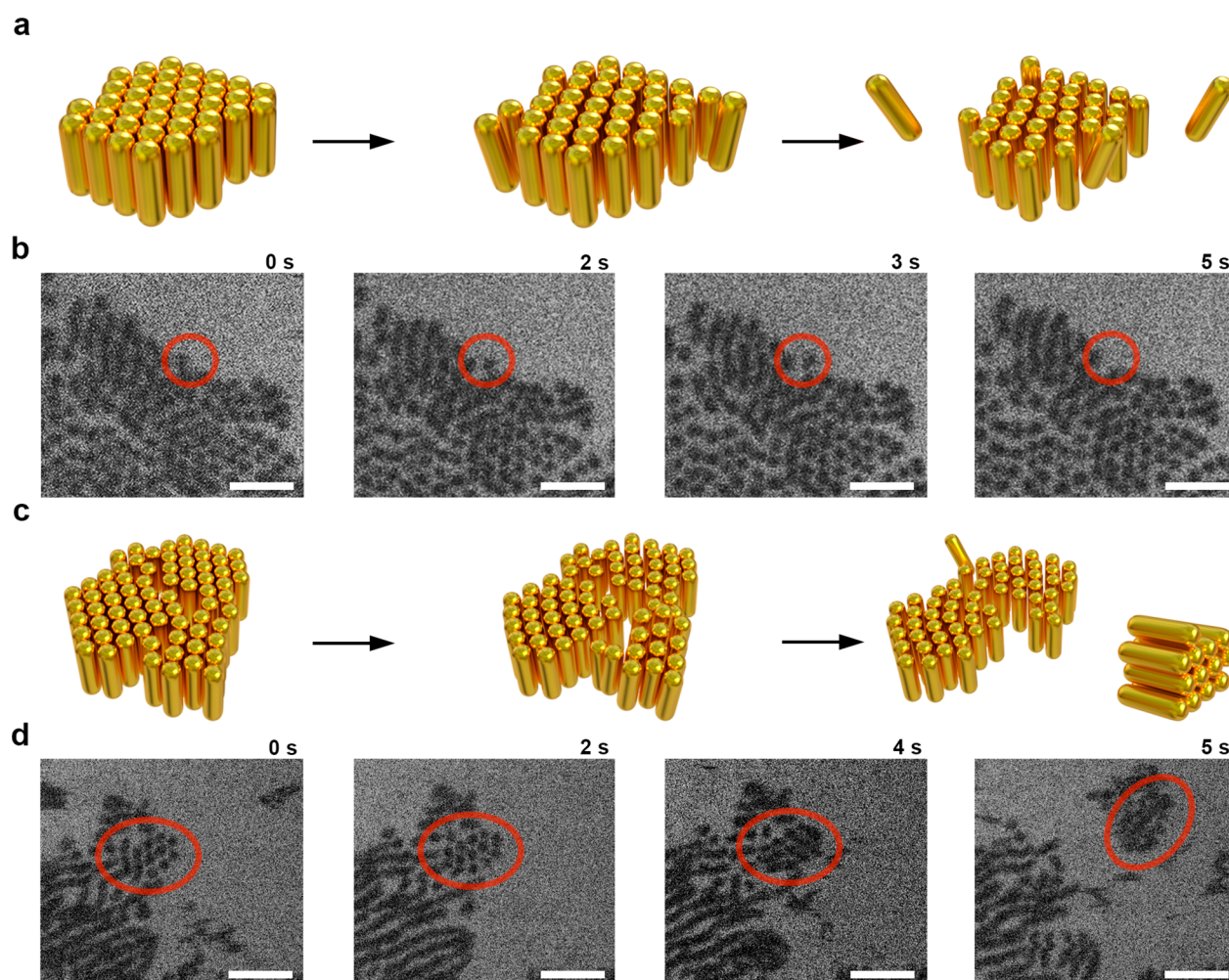


Figure 3. WetSTEM characterization of AuNR@MUDOL. (a) Schematic model of vertically aligned AuNR@MUDOL and single nanoparticle displacement events. (b) WetSTEM images of an AuNR@MUDOL vertical aggregate, showing a single nanoparticle detaching from the aggregate. In the first three frames, we highlight an area containing three AuNRs; after 5 s one AuNR is seen to leave the aggregate (Movie S1). (c) Schematic representation of the observed AuNR@MUDOL behavior, displacement and movements of vertically ordered AuNR clusters. (d) WetSTEM images of an AuNR@MUDOL vertical aggregate, showing an example of AuNR cluster displacement; the apparent changes in cluster appearance are due to variations in the orientation of nanorods in respect to the observation direction; this effect evidence dynamic movements of small side-to-side, 2D ordered clusters (Movie S2).

175 **Bulk Investigation of the Dynamic Self-Assembly of**
 176 **AuNR@MUDOL.** Compounds comprising polymeric and
 177 oligomeric ethylene glycol moieties are known to exhibit
 178 thermoresponsive behavior.^{37–39} In the case of self-assembled
 179 monolayers, a temperature increase can lead to change of intra-
 180 and intermolecular interactions and enable more efficient
 181 interactions with water molecules.⁴⁰ Thus, when the formation
 182 of a precipitate was observed by eye (Figure 2a) in an aged
 183 sample of AuNR@MUDOL, we proceeded to heat it and
 184 watch whether the nanoparticles get thereby redispersed.
 185 Indeed, after heating for 10 min, we observed that the color of
 186 the dispersion turned purple, similar to that observed right
 187 after ligand exchange, thus confirming the reversibility of self-
 188 assembly. The time required to observe AuNR disassembly was
 189 of only tens of seconds if sonication was used additionally to
 190 heating. Importantly, our experiments confirm that the
 191 assembly process can be reversed, however, after 3 consecutive
 192 cycles of UV/vis measurements revealed a 4 nm redshift and
 193 20% decrease of intensity of the longitudinal LSPR band
 194 (Supplementary Note 1).

To study in detail the reversibility of the self-assembly of
 AuNR@MUDOL, we used small angle XRD (SAXRD). AuNR@MUDOL
 were initially dispersed in water, which intrinsically limited the
 temperature range for the measurements. Therefore, we transferred
 AuNR@MUDOL into glycerol, which has similar dielectric prop-
 erties to water but a higher boiling point. AuNR@MUDOL in glycerol
 was allowed to precipitate and then carefully transferred to a glass
 capillary for temperature-dependent SAXRD measurements. We first
 collected 1D diffractograms at 30 °C (Figure 2b), which revealed
 the presence of several Bragg peaks, indicating the formation of
 long-range ordered assemblies. This pattern was fitted using a
 2D hexagonal unit cell, with a dimension (nearest neighbor distance
 between nanoparticles) of ~22 nm. This is slightly longer than the
 value derived from TEM (~20 nm), in agreement with the dry state
 of the samples in TEM, while glycerol as a solvent may infiltrate
 in between the nanoparticles.⁴¹ Hexagonal packing of AuNRs
 within vertical assemblies has been previously reported, for both
 monolayers and complex, 3D smectic assemblies.¹² In our SAXRD
 measurements, we did not observe peaks corresponding to 215

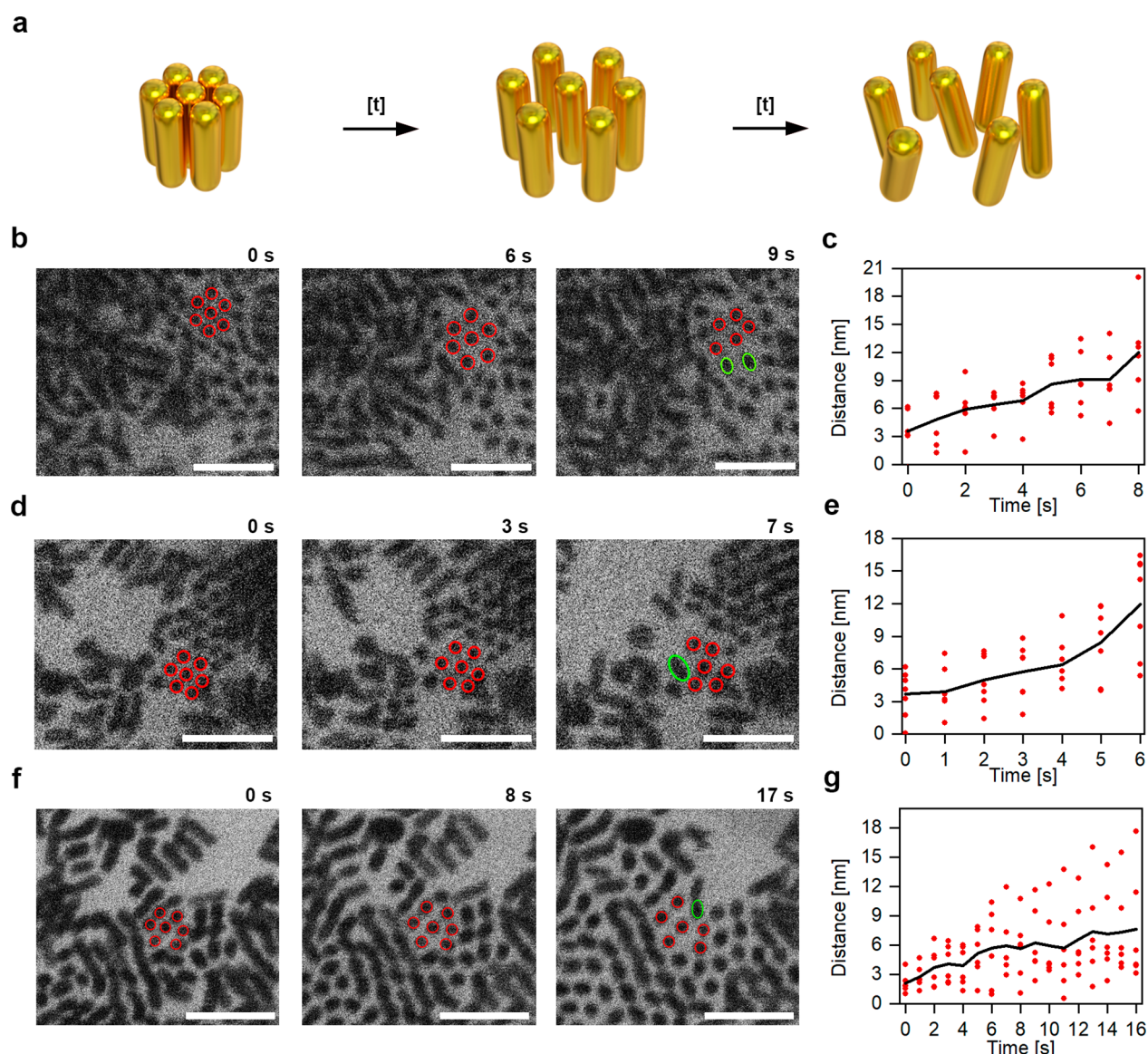


Figure 4. WetSTEM characterization of orientational order within AuNR@MUDOL aggregates. (a) Schematic model of the observed phenomena. (b,d,f) Time-lapse images from in situ WetSTEM recordings of the disassembly of an AuNR@MUDOL aggregate; AuNR clusters for which calculations of interparticle distances were performed are highlighted with red circles; green circles highlight tilted AuNRs, which lost their initial orientational correlation with respect to the rest of the cluster (Movies S6–S8). (c,e,g) Evolution of interparticle distance (surface-to-surface) within the clusters imaged in (b,d,f). Red dots represent distances between pairs of AuNRs, while the solid black line is the averaged value.

216 multilayer stacking of nanorods, but it should be noted that
217 this signal would appear at angles beyond the sensitivity of our
218 in-house SAXRD instrument.

219 We then performed temperature-dependent SAXRD meas-
220 urements. The sample was heated from 30 °C up to 200 °C
221 and diffractograms were collected every 10 °C (Figure 2c). To
222 prevent heat-induced nanoparticle degradation, the acquisition
223 time was kept relatively short (60 s), and therefore we focused
224 on following the evolution of the main (10) Bragg peak, which
225 was visible up to ~135 °C. When approaching this
226 temperature, the peak intensity lowered, indicating a slow
227 disintegration of the aggregates (lower nanoparticle correlation
228 length). Above 135 °C no sharp Bragg peaks were observed
229 but only a broad scattering around the primary beam, which
230 evidenced an isotropic distribution of nanoparticles in the
231 solvent, without orientational order. These results confirm our
232 initial bulk-scale observations.

Nanoscope Investigation of the Dynamic Self- 233
Assembly of AuNR@MUDOL. To study the self-assembly 234
of AuNR@MUDOL in more detail, we employed in situ 235
electron microscopy imaging of the particles in a liquid. In 236
contrast to TEM-based methods for the examination in liquid, 237
WetSTEM does not require the use of microfluidic devices. We 238
simply drop-casted a dispersion of AuNR@MUDOL in water/ 239
glycerol (1:1 v/v) on top of a standard carbon-coated TEM 240
grid and placed it inside a precooled STEM device. The use of 241
a water/glycerol suspension ensured similar conditions to 242
those previously used in bulk SAXRD measurements. 243
However, a much lower temperature of 2 °C and a reduced 244
pressure of 700 Pa were used in WetSTEM experiments, which 245
made the comparison with bulk measurements less accurate. 246
As a first observation, we confirmed the tendency of AuNR@ 247
MUDOL to self-assemble into vertically oriented arrays 248
(Figure 3), in agreement with TEM imaging of samples 249 3

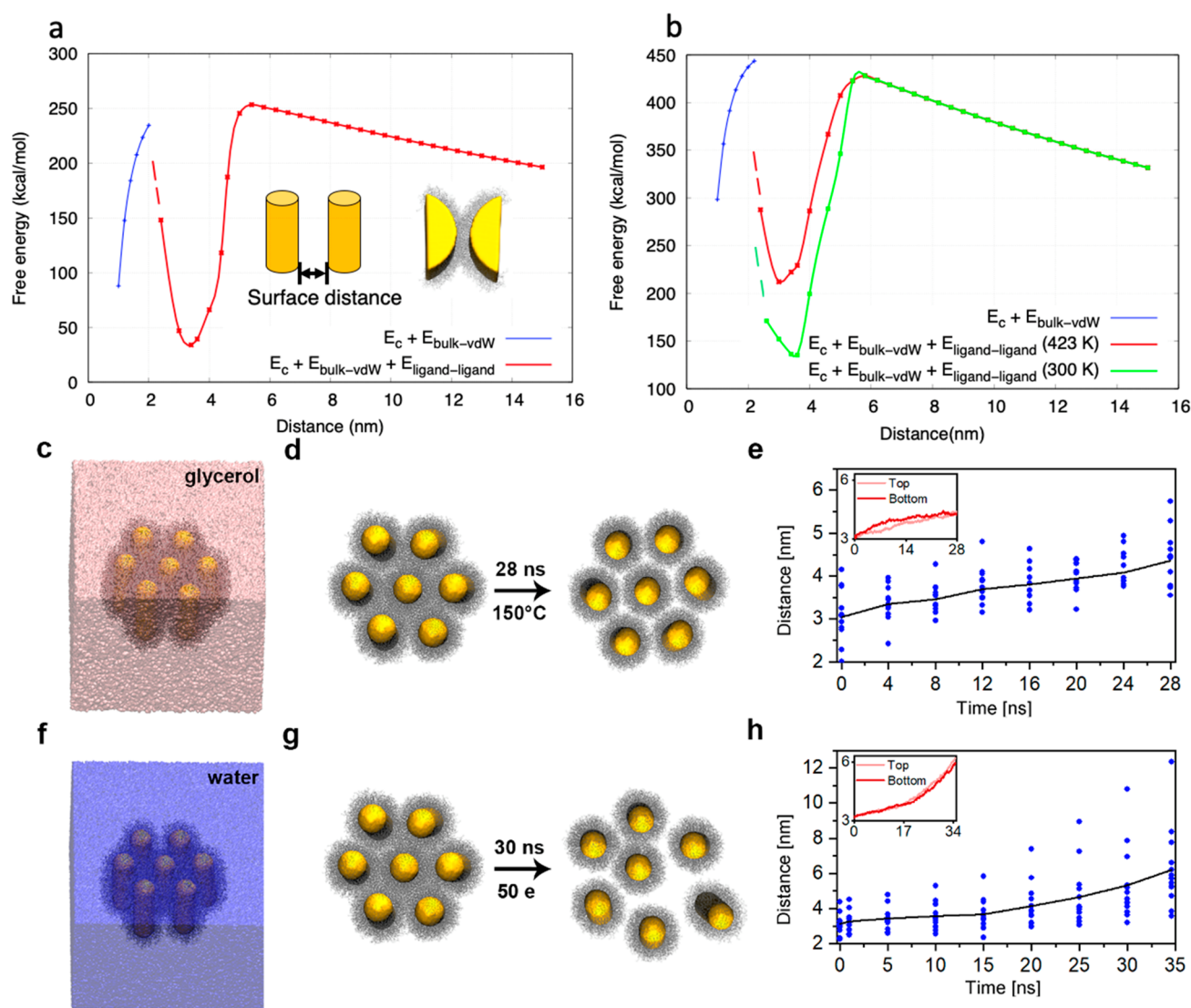


Figure 5. Mean-field modeling of the interactions between AuNRs and MD simulations of stimuli-driven disassembly of small AuNR@MUDOL clusters. (a) Total interaction free energy ($E_{\text{vdW}} + E_C + E_{\text{ligand-ligand}}$, red dots) at 300 K between AuNRs (52×16 nm) with water as solvent and 130 e charge on the NRs. Solid lines are given for eye guidance. In the right inset two 5 nm-thick slices from 52×16 nm AuNRs at a surface distance of 3.6 nm are shown, which were considered in the MD simulation to estimate the ligand–ligand coupling. Solvent molecules are removed for clarity. (b) Total interaction free energy ($E_{\text{vdW}} + E_C + E_{\text{ligand-ligand}}$) at two different temperatures (27 and 150 °C), between AuNRs (52×16 nm) in glycerol, assuming 130 e charge on the NRs. Solid lines are given for eye guidance. (c) Corner-view of small AuNRs fully submerged in glycerol at 25 °C. (d) Disassembly of small neutral AuNRs at high temperature (150 °C) in glycerol (snapshots from [Movie S9](#)). (e) Time evolution of distances between AuNRs (surface-to-surface) within an AuNR cluster at high temperature (150 °C) in glycerol (data corresponding to the simulation shown in panel d). Blue dots represent distances between pairs of AuNRs, while the solid black line is the averaged value. (inset) The same time-dependent averaged distances are shown separately for the top and bottom ends of AuNRs. (f) Corner-view of the small AuNRs on the surface of water at 25 °C. (g) Disassembly of small charged (50 e) AuNRs in bulk water at 25 °C (snapshots from [Movie S10](#)). (h) Time evolution of the distances between charged AuNRs (surface-to-surface) within an AuNR cluster in bulk water at 25 °C. (inset) The same time-dependent averaged distances are shown separately for the top and bottom ends of AuNRs (data corresponding to the simulation shown in panel g).

250 prepared at ambient pressure. Second, we consistently
 251 observed fluctuations of the nanoparticles within the
 252 solvent–trembling, twisting, assembling, and disassembling–
 253 often similar to previous reports based on the in situ TEM
 254 method.²⁷ Third, we could monitor the displacement of
 255 individual nanorods (see schematic drawings in [Figure 3a](#), still
 256 images from WetSTEM recordings in [Figure 3b](#), and [Movie S1](#)
 257 in the Supporting Information), in particular those which were
 258 located at the edges of vertical aggregates. These observations
 259 correlate well with the bulk-scale observations of thermally
 260 driven disassembly for AuNR@MUDOL aggregates and
 261 confirm that we can analyze the process with single-particle

precision. In summary, we can safely assume that the 262
 WetSTEM experimental conditions are suitable to monitor 263
 the dynamic behavior of Au nanorods, which is similar to their 264
 macroscale behavior. 265

Close observation of the vertical assemblies of AuNR@ 266
 MUDOL allowed us to register, apart from the displacement of 267
 individual AuNRs, the detachment, and movement of side-to- 268
 side ordered clusters comprising tens of nanoparticles ([Figure](#) 269
[3c,d](#), and [Movie S2](#)). Importantly, despite the clusters' dynamic 270
 behavior (twisting/turning, finally “swimming” away), AuNRs 271
 therein maintained their initial orientational order. Schematic 272
 models and images from three such events are shown in [Figure](#) 273

274 3c, d (see more examples in the SI, Figure S3a-b and SI Movies
275 S3–S4). This is a striking in situ observation of the colloidal
276 behavior of ordered, relatively large (more than 10 nano-
277 particles) AuNR clusters. The colloidal stability of such
278 clusters is in agreement with the above UV/vis spectra (Figure
279 1d) and with the proposed mechanism for the formation of
280 vertical AuNR assemblies, in which side-to-side aggregates are
281 first formed, followed by precipitation from the dispersion and
282 arrangement on a substrate. This behavior also indicates that in
283 our experimental conditions the solvent layer is thick enough
284 to fully cover vertically aligned AuNRs.

285 We thus conclude that observations of the dynamic behavior
286 of AuNRs in the wet state, at the bulk- and the nanoscale, can
287 be correlated. In both cases, disassembly of AuNR aggregates
288 can be monitored, even though the underlying principles differ.
289 In the SAXRD measurements, disassembly is induced by an
290 increase in temperature (thermal energy), whereas in
291 WetSTEM measurements electrostatic interactions (electron
292 beam induced charging of the sample) are likely to provide the
293 main driving force for disassembly, since electron beam
294 induced heating effects are negligible^{42,43} (Supplementary
295 Note 2). Given the observed similarities, we investigated the
296 disassembly process of AuNR vertical aggregates from
297 WetSTEM movies. We noted a gradual increase in the
298 distance between AuNRs, under the influence of the electron
299 beam. AuNRs were consistently seen to drift apart from each
300 other prior to rapid disassembly of the clusters into individual
301 AuNRs. Although a detailed analysis of this process within a
302 moving cluster (previously discussed) proved challenging, we
303 could monitor the evolution of larger assemblies.^{44,45}

304 Therefore, we focused on disassembly events occurring in
305 2D vertical assemblies, for which AuNRs keep their orientation
306 with respect to the electron beam axis. To minimize differences
307 between observations of separate events we identified
308 assemblies comprising well-ordered clusters made of seven
309 hexagonally arranged nanorods. A schematic model for the
310 process and selected time-lapse frames from sample recordings
311 are shown in Figure 4. These in situ WetSTEM observations
312 allowed us to draw two main conclusions. First, the process of
313 increasing interparticle spacing can be commonly observed in
314 the prepared samples. Second, after reaching a critical
315 interparticle distance, AuNRs start to tremble rapidly and
316 end up losing orientational correlation within their original
317 cluster (Figure 4, multiple such events can be found in Movie
318 S5). We can, therefore, image the evolution of orientational
319 order in clusters of anisotropic nanoparticles, using an in situ
320 EM method. To get a more detailed picture, we quantified our
321 observations by monitoring 2D, hexagonally close-packed
322 structures and calculated the mean separation distance
323 (surface-to-surface) between a central AuNR and six
324 surrounding neighbors forming a 2D hexagonal close-packed
325 structure in the initial state (Figure 4b,d,f and Movies S6–S8).
326 The starting distance, 3–5 nm (Figure 4c,e,g), correlates well
327 with the interparticle distances calculated from SAXRD
328 measurements after subtracting the AuNRs diameter. Under
329 the electron beam, we witnessed an increase of interparticle
330 distance within seconds, accompanied by trembling of AuNRs,
331 while their average positional order was maintained. The loss
332 of orientational correlation between AuNRs was observed at
333 interparticle distances of 7–12 nm, which are slightly larger
334 than twice the length of an extended MUDOL ligand.
335 Although several factors, such as the presence of neighboring
336 AuNRs, electron beam intensity (at different imaging

magnifications), and thickness of the solvent layer, may
337 influence the distance at which positional order is lost, the
338 values estimated on the basis of different recordings are in
339 good agreement. 340

To understand better the self-assembly and disassembly of
341 the experimental AuNR@MUDOL, we performed hybrid
342 multiscale (MS) modeling of large AuNRs (52 × 16 nm) and
343 separate molecular dynamics (MD) simulations of the
344 disassembly dynamics in small model AuNRs@MUDOL (13
345 × 4 nm). 346

MS modeling in Figure S4a shows that the large AuNRs
347 have a significant bulk vdW attraction, giving a potential well of
348 ~22 kcal/mol at their surface distances of 3–4 nm. In contrast,
349 small AuNRs have a rather small vdW barrier of a few kcal/
350 mol, which means that their short-range attraction mostly
351 originates from ligand–ligand coupling. These results suggest
352 that AuNRs should self-assemble in water at room temperature
353 due to bulk vdW coupling, and it is unlikely that they would
354 separate without additional repulsion, discussed below. 355

In Figure S4a, we show the coupling potential energies of
356 large AuNRs with 10 to 130 electron charges per NR. 357

Figure S4b shows that the repulsive Coulombic coupling
358 between large charged NRs can decrease the above vdW
359 barrier. To examine how the potential energy wells shown in
360 Figure S4b change when ligand–ligand coupling is included,
361 we performed molecular modeling of large AuNRs coated with
362 MUDOL ligands. The ligand–ligand coupling free energy
363 between two AuNR at different surface distances (2.4–5.4
364 nm), submerged in both water and glycerol, were calculated
365 using solvation free energy calculation with MM/GBSA. For a
366 given NRs distance, the ligand–ligand coupling energies
367 depend on the ligand density and the NRs spatial overlap.
368 For simplicity, the coupling energies are calculated from 5 nm
369 slices of two 52 × 16 nm AuNRs solvated in water ($T = 300$ K)
370 and glycerol ($T = 300$ and 423 K), as shown in Figure 5a (inset
371 on the right). 372

Figure 5a shows the total interaction free energies ($E_{\text{vdW}} +$
373 $E_{\text{C}} + E_{\text{ligand-ligand}}$) of AuNRs (with 130 e charge) submerged in
374 water at 27 °C (300 K). In this case, a potential well of ~220
375 kcal/mol is detected, which needs to be overcome for the
376 disassembly process to occur. In Figure 5b, we also show
377 calculated total potential energies for AuNRs submerged in
378 glycerol. Note that the potential energy well of the system at
379 150 °C is reduced by 25%, as compared to the system at 27 °C.
380 This clearly indicates a temperature-induced entropic repulsion
381 of the ligands, which can promote disassembly. 382

To examine more closely the disassembly dynamics of
383 AuNRs, we performed MD simulations of a hexagonal cluster
384 made of seven small model AuNR@MUDOL, while neglecting
385 their bulk vdW coupling (Supplementary Note 3 and Figure
386 S5). The simulations were performed at different temperatures
387 and in different solvents. 388

The experimental AuNR@MUDOL solvate better in
389 glycerol, where they disassemble above 135 °C. The
390 disassembly AuNRs might be promoted by entropic effects
391 and NRs charging, leading to a relatively strong repulsion in
392 glycerol. On the other hand, small neutral AuNRs, with partly
393 hydrophobic ligands self-assemble at 25 °C on the water
394 surface, with their tips partly exposed and a surface-to-surface
395 distance of 3 nm, stabilized by ligand–ligand coupling. This
396 AuNR arrangement was used as the starting point for our
397 stimuli-driven disassembly simulations in which we heated the
398 system or charged the small AuNRs to understand their
399

400 disassembly dynamics and compare it with the experimental
401 results (Supplementary Notes 4–6).

402 We simulated small neutral AuNRs@MUDOL submerged in
403 glycerol at 25 and 150 °C (Supplementary Note 4). Whereas
404 in the former case we did not observe disassembly of AuNRs
405 (Figure S6), in the latter (after 28 ns) we did observe their
406 gradual disassembly (Figure Sd and Movie S9). Figure Se
407 shows that the distance between AuNRs increases from ~3.0
408 to 4.3 nm. From the experimental point of view, the increased
409 separation distance (5 nm) at higher temperatures (due to
410 entropic ligand repulsion) could be sufficiently advantageous
411 (energetically) for them to overcome the combined vdW and
412 Coulombic barrier (Figure S4b). Larger thermal fluctuations
413 also participate in this process, which can be seen from the
414 evolution of interparticle distances between the top and
415 bottom parts of the nanorods (inset, Figure Se).

416 Finally, we addressed the effect of AuNR charging on the
417 self-assembly process. Therefore, we simulated the process for
418 in situ WetSTEM experiments, where we would not expect
419 heating of the solution, so we could investigate the disassembly
420 of AuNRs induced by e-beam-induced charging (Supplemen-
421 tary Note 5). When considering a charge of 20 e per small
422 AuNR@MUDOL partly or fully submerged in water, no
423 disassembly was observed (Figure S7a-d). However, when
424 charged with 50 e per AuNR@MUDOL, for the fully
425 submerged case, gradual disassembly occurred (Figure 5g
426 and Movie S10). Their average surface-to-surface distance
427 increased from the initial ~3.0 up to 6.1 nm (Figure 5h), while
428 trembling similarly to our in situ experimental observations
429 (inset, Figure 5h). The AuNRs orientation became more
430 disorganized when their separations became roughly twice the
431 ligand length. A similar outcome was observed for AuNRs with
432 the same 50 e charge, which were partially submerged in water
433 (Figure S7e,f). In this case, a radial, more symmetrical path
434 toward AuNRs disassembly was evidenced, which allows
435 AuNRs to keep a hexagonal order during disassembly. In
436 contrast, a more chaotic behavior was evidenced for fully
437 submerged AuNRs, in which the hexagonal order is lost. The
438 latter was observed in real electron microscopy measurements,
439 suggesting that we could probe the dynamics of assemblies that
440 were fully submerged in the solvent. To maximize the
441 generality of our theoretical framework, we performed
442 additional simulations of AuNR@MUDOL partly or fully
443 submerged in water at 100 °C and observed that these systems
444 did disassemble (Supplementary Note 6, Figure S8a-d, and
445 Table S1). We should keep in mind that despite the dynamics
446 of experimental (large) and MD-simulated (small) NRs are
447 qualitatively similar at the same temperatures and in the same
448 solvents, the disassembly time scales and necessary NRs
449 charging might be much larger in the experimental (large)
450 NRs. That can be clearly expected from the deep potential
451 wells shown in Figure 5 a,b.

452 It is intriguing to think that, in the context of the
453 experimentally confirmed reversibility of the disassembly
454 process (Figure 2), reversing time in our recordings would
455 enable us to get insight into the assembly process—assembly of
456 single particles as well as clusters of ordered AuNRs
457 (Supporting Information, Movies S11–S12), which is similar
458 to the pre- and postattachment alignment pathways²⁷
459 previously reported in the literature for side-to-side assemblies
460 of AuNRs.

CONCLUSIONS

461

In summary, we carried out a comprehensive study of the
462 (stimuli-responsive) self-assembly of gold nanorods function-
463 alized with MUDOL ligands, into vertical arrays. In situ
464 WetSTEM imaging provided us with a unique, direct insight
465 into this process, showing strong evidence (formation of
466 vertical arrays, and movements of AuNRs) that in situ
467 observations at the single particle level are in agreement with
468 bulk measurements. Notably, we obtained direct proof of the
469 colloidal stability of side-to-side, 2D assemblies of AuNRs,
470 even when in motion. Our approach also allowed us to
471 monitor the disassembly process, which first proceeds with
472 AuNRs keeping orientational order, subsequently losing order
473 after separating to distances larger than double the length of
474 MUDOL ligands. Multiscale modeling enabled us to in silico
475 recreate the thermal- and charge-driven disassembly of AuNRs
476 and to analyze these processes in the context of vdW,
477 Coulombic, and thermal interactions between AuNRs. In
478 conclusion, this work highlights the versatility of the
479 WetSTEM imaging technique for in situ EM studies of NP
480 dynamics and provides insight into the stability orientationally
481 ordered NR assemblies. 482

EXPERIMENTAL SECTION

483

Materials. All chemicals were used as received, with no further
484 purification. Gold(III) chloride hydrate (HAuCl₄·H₂O, 99.995% trace
485 metals basis), hexadecyltrimethylammonium bromide (CTAB,
486 ≥98%), sodium borohydride (NaBH₄, powder ≥98%), silver nitrate
487 (AgNO₃, ACS reagent, ≥99.0%), 1-mercaptoundec-11-yl)hexa-
488 (ethylene glycol (MUDOL, 90%), and glycerol (ACS reagent,
489 ≥99.5%), were all purchased from Sigma-Aldrich. Milli-Q water
490 (resistivity 18.2 MΩ cm at 25 °C) was used in all experiments. All
491 glassware was washed in aqua regia. 492

Synthesis of Gold Nanorods. AuNR@CTAB. Gold nanorods
493 were prepared following a previously reported seed-mediated
494 method.²⁹ In the first step, seeds were prepared as follows: 25 μL
495 of a 0.05 M HAuCl₄ solution was added to 4.7 mL of 0.1 M CTAB
496 solution and, after 5 min, 300 μL of a 0.01 M NaBH₄ (freshly
497 prepared) solution was injected under vigorous stirring. Then, 120 μL
498 of seed solution was injected to the growth solution containing CTAB
499 100 mM, HAuCl₄ 0.5 mM, AgNO₃ 0.04 mM and ascorbic acid 0.75
500 mM (total volume: 10 mL). The reaction was allowed to proceed
501 undisturbed for 2 h at 30 °C. The obtained AuNRs were on average
502 51 nm inside length and 15 nm in thickness. 503

Ligand Exchange on AuNRs. AuNR@MUDOL. A total of 1 mL
504 of MUDOL solution (0.5 mM) was added to 10 mL of Au NRs
505 dispersion (1 mg/mL) in 5 mM CTAB. The reaction mixture was
506 sonicated for 30 min and left under mild stirring overnight. Then, the
507 solution was centrifuged at 3000 rpm for 10 min and the precipitate
508 was redispersed in 2 mL of 5 mM CTAB solution. To transfer
509 AuNR@MUDOL to glycerol, the aqueous dispersion was centrifuged
510 at 3000 rpm for 10 min, and the precipitate redispersed in glycerol
511 under sonication. 512

Assemblies of Nanorods. For structural analysis, AuNR@
513 MUDOL precipitate was placed in a glass capillary for small angle
514 X-ray diffraction (SAXRD) analysis. Measurements were performed
515 with a Bruker Nanostar system (Cu Kα radiation, parallel beam
516 formed by cross-coupled Goebel mirrors, and a 3-pinhole collimation
517 system, VANTEC 2000 area z detector). Fitting of the obtained
518 diffractogram and simulation of the patterns was performed with
519 Topas 3 software (Bruker). Transmission electron microscopy
520 analysis of AuNRs was performed using TEM model JEM-1400
521 (JEOL, Japan), available in Nencki Institute of Experimental Biology,
522 Laboratory of electron microscopy. Samples were prepared by drop-
523 casting small aliquots of the as obtained dispersions of AuNRs onto
524 TEM grid, then left to dry under ambient conditions. Spectroscopy in 525

526 the UV–vis range studies was performed using GENESYS 50 UV–vis
527 spectrophotometer, available at University of Warsaw.

528 **Modeling Plasmonic Properties of AuNR Assemblies.** The
529 Finite-Difference Time-Domain (FDTD) method30 (Lumerical
530 Solutions, Inc.) was used to model the optical properties of single
531 Au NRs and small clusters thereof. All simulations were performed in
532 water (refractive index 1.33). The nanorod dimensions were selected
533 to fit the experimental sample. Dielectric data for gold were obtained
534 by fitting experimental data from Johnson and Christy⁴⁷ (0.220 RMS
535 error). All simulations were terminated after reaching a shutoff level of
536 10^{-6} .

537 **In Situ Electron Microscopy (WetSTEM) Observations.** The
538 wet scanning transmission electron microscopy (WetSTEM) system is
539 tailored for high-resolution imaging under conditions of mild pressure
540 and provides the opportunity for in situ dynamic imaging of liquid
541 samples. We used a QUANTA SEM 250 FEG/FEI, equipped with a
542 field emission gun (FEG) system, containing detectors tailored for
543 scanning and transmission imaging in bright- and dark-field. The grid
544 holder is designed for standard 3 mm TEM grids. Furthermore, it
545 provides the possibility to fully control the conditions in the specimen
546 chamber, in terms of temperature and pressure. Our observations
547 were usually carried out at 2 °C, with pressure between 700–1000 Pa,
548 at a landing voltage of 30 kV and low electron flux ranging from 2 to
549 $17e \text{ (}\text{Å}^2 \text{ s)}^{-1}$ (Supplementary Note 2), which makes the effect of
550 water radiolysis negligible.^{48,49} Since the study was performed on
551 TEM grids, we minimized the impact of electrons backscattered from
552 the support, which could be expected in a regular SEM setup. In a
553 typical experiment, to 100 μL of dispersion of AuNR@MUDOL was
554 added 15 μL of glycerol. Then, an aliquot of the mixture was drop-
555 casted onto a TEM grid previously fixed on the cold (0 °C) WetSEM
556 holder, to make sure that water would not evaporate before closing
557 the equipment and lowering the pressure. After equilibration of the
558 grid for 1 min, the specimen chamber was sealed and the pressure
559 inside was quickly lowered to 1200 Pa and then slowly (10 Pa step)
560 lowered to 700 Pa, to acquire optimal conditions for imaging (lowest
561 obtainable pressure with water remaining in the liquid state on top of
562 the TEM grid). After stabilizing the conditions inside the chamber,
563 the electron beam was turned on for imaging. Videos were recorded at
564 a rate of 50 ns per pixel, with a GSED detector.

565 **Simulation Methods.** Self-assembly and disassembly processes of
566 AuNRs were described by hybrid multiscale (MS) modeling for
567 realistic AuNRs, as well as molecular dynamics (MD) simulations for
568 smaller AuNR@MUDOL. Different competing interactions act
569 between solvated AuNRs, such as bulk van der Waals (vdW)
570 coupling, mean electrostatic coupling, ligand–ligand coupling, etc.
571 The effects associated with long-range interactions between AuNRs
572 are captured by the MS method, while their short-range interactions
573 are better described by the MD method.

574 **Multiscale Modeling.** Using multiscale methods, we calculated
575 bulk vdW coupling energies E_{vdW} (bulk material of AuNRs), mean
576 electrostatic interaction energies E_{c} (overall AuNR charging), and
577 atomistic ligand–ligand coupling energies $E_{\text{ligand–ligand}}$ between pairs of
578 realistic AuNRs (52 \times 16 nm) as a function of their separation in
579 different solvents.

580 The bulk vdW coupling energy, E_{vdW} , between two AuNRs (52 \times
581 16 nm) was calculated by the Hamaker summation (1) over their
582 volume elements,

$$E_{\text{vdW}} = -\frac{A}{\pi^2} \iint \frac{1}{|r_1 - r_2|^6} dr_1 dr_2 \quad (1)$$

584 Here A is the Hamaker constant for Au–Au interaction in water ($A =$
585 1.80 eV), and r_1 and r_2 are the position vectors of volume elements on
586 both NRs.

587 The electrostatic interaction energy, E_{c} , was calculated by summing
588 over pairs of charged elements, each taken from one of the considered
589 AuNRs, homogeneously distributed on the AuNR surface (modeled
590 as a cylinder) with a thickness 0.5 nm (2),

$$E_{\text{c}} = \iint \frac{\rho(r_1)\rho(r_2)}{4\pi\epsilon_0\epsilon|r_1 - r_2|} dr_1 dr_2 \quad (2)$$

Here $\epsilon = 80$ is the dielectric constant of water, $\rho(r_{1,2})$ is a charge
592 density at the position $r_{1,2}$, and $|r_1 - r_2|$ is the distance between both
593 charged elements.
594

Atomistic Molecular Dynamics Simulations. We have
595 separately simulated the disassembly dynamics in small AuNRs (13
596 \times 4 nm) covered with 300 neutral MUDOL molecules and solvated
597 in water (bulk or surface) and glycerol ($400 \times 400 \times 200 \text{ Å}^3$ or $400 \times$
598 $400 \times 340 \text{ Å}^3$ boxes). AuNR@MUDOL were simulated with
599 Nanoscale Molecular Dynamics (NAMD)⁴⁶ in NVT (partially
600 exposed AuNRs, 3 simulations) or NPT (fully submerged AuNRs,
601 5 simulations) ensembles at $T = 300, 373,$ and 423 K , using the
602 Langevin dynamics with a damping constant of $C_{\text{Lang}} = 0.1 \text{ ps}^{-1}$ and a
603 time step of 2 fs. The CHARMM general force field^{50,51} was
604 implemented for the bond, angle, and dihedral parameters of the
605 ligands and solvent molecules. The electrostatic coupling between
606 ions and partially charged atoms (nonbonding interactions) has a
607 cutoff of 1 nm, but the long-range part of this coupling was calculated
608 by the PME method⁵² (under periodic boundary conditions).
609 Nonbonding vdW attraction and steric repulsion between molecules
610 were described by Lennard-Jones (LJ) potentials (3),
611

$$U_{\text{LJ}}(r) = \epsilon \left[\left(\frac{r_{\text{min}}}{r} \right)^{12} - 2 \left(\frac{r_{\text{min}}}{r} \right)^6 \right] \quad (3)$$

where ϵ is the minimum (negative) energy of this coupling and r_{min} is
613 a distance at which $U_{\text{LJ}}(r_{\text{min}})$ has a local minimum, as provided by the
614 CHARMM force field. The LJ potential implemented in NAMD has a
615 typical cutoff distance of 1 nm (within the solvent).
616

We also used the atomistic molecular dynamics simulations to track
617 the free energies derived from coupling of segments in large NRs,
618 including ligand–ligand interactions. Toward this end, we constructed
619 a 5 nm-thick slice from two $52 \times 16 \text{ nm}$ (right inset, Figure 5a)
620 AuNRs coated with MUDOL ligands and submerged in either water
621 (300 K) or glycerol (300 and 423 K). The solvent box in the
622 simulation had dimensions of $320 \times 320 \times 50 \text{ Å}^3$. The system was
623 first constructed with a surface distance of 5.4 nm. Then, we applied
624 force on one slice, fixed the other slice, and let them approach each
625 other in short simulations. At the desired surface distances, we saved
626 the systems, froze the slices (bulk material) except ligands, and
627 performed MD simulations (described above) on each system for
628 another 10 ns. We then calculated ligand–ligand coupling free
629 energies between the slices (height = 5 nm, diameter = 16 nm) at
630 different surface distances (2.4–5.4 nm) between NRs using solvation
631 free energy calculations with the MMGB-SA method.^{53,54} The free
632 energies were averaged over the last 5 ns of the trajectory.
633

Free energies were estimated from separate MMGB-SA calculations
634 for three systems (two separate AuNR@MUDOL and the self-
635 assembled AuNR@MUDOL complex) in the configurations extracted
636 from the MD trajectories of the whole complex in the given solvent.
637 Then, coupling free energies of NRs were calculated from
638

$$\Delta G_{\text{bind}} = G_{\text{GBSA}}(\text{complex}) - G_{\text{GBSA}}(\text{separate NRs1}) \\ - G_{\text{GBSA}}(\text{separate NRs1})$$

Free energies were calculated using NAMD 2.13 package
639 generalized Born implicit solvent model,⁵⁵ with a dielectric constant
640 of the solvent of 80 and 46.5. The nonpolar contribution for each
641 system configuration was calculated in NAMD as a linear function of
642 the solvent-accessible surface area (SASA), determined using a probe
643 radius of 1.5 Å with a surface tension of $\gamma = 0.00542 \text{ kcal/mol Å}^{-2}$.
644

■ ASSOCIATED CONTENT

Supporting Information

The Supporting Information is available free of charge at
647 <https://pubs.acs.org/doi/10.1021/jacs.0c06446>.
648

649 Supplementary figures and supplementary notes on MD
650 simulations 1–6 (PDF)
651 Recording from WetSTEM measurements (Movie S1)
652 (MP4)
653 Recording from WetSTEM measurements (Movie S2)
654 (MP4)
655 Recording from WetSTEM measurements (Movie S3)
656 (MP4)
657 Recording from WetSTEM measurements (Movie S4)
658 (MP4)
659 Recording from WetSTEM measurements (Movie S5)
660 (MP4)
661 Recording from WetSTEM measurements (Movie S6)
662 (MP4)
663 Recording from WetSTEM measurements (Movie S7)
664 (MP4)
665 Recording from WetSTEM measurements (Movie S8)
666 (MP4)
667 Video from MD simulations (Movie S9) (MPG)
668 Video from MD simulations (Movie S10) (MP4)
669 Recording from WetSTEM measurements (Movie S11)
670 (MP4)
671 Recording from WetSTEM measurements (Movie S12)
672 (MP4)

673 ■ AUTHOR INFORMATION

674 Corresponding Authors

675 **Petr Král** – Department of Chemistry and Department of
676 Physics, Biopharmaceutical Sciences, and Chemical Engineering,
677 University of Illinois at Chicago, Chicago, Illinois 60607, United
678 States; orcid.org/0000-0003-2992-9027; Email: [pkral@](mailto:pkral@uic.edu)
679 [uic.edu](mailto:pkral@uic.edu)

680 **Wiktor Lewandowski** – Laboratory of organic nanomaterials
681 and biomolecules, Faculty of Chemistry, University of Warsaw,
682 Warsaw 02-093, Poland; CIC biomaGUNE, Basque Research
683 and Technology Alliance (BRTA) and CIBER-BBN, Donostia,
684 San Sebastián 20014, Spain; [orcid.org/0000-0002-3503-](https://orcid.org/0000-0002-3503-2120)
685 [2120](mailto:wlewandowski@chem.uw.edu.pl); Email: wlewandowski@chem.uw.edu.pl

686 **Luis M. Liz-Marzán** – CIC biomaGUNE, Basque Research and
687 Technology Alliance (BRTA) and CIBER-BBN, Donostia, San
688 Sebastián 20014, Spain; Ikerbasque, Basque Foundation for
689 Science, 48013 Bilbao, Spain; [orcid.org/0000-0002-6647-](https://orcid.org/0000-0002-6647-1353)
690 [1353](mailto:llizmarzan@cicbiomagune.es); Email: llizmarzan@cicbiomagune.es

691 Authors

692 **Dorota Grzelak** – Laboratory of organic nanomaterials and
693 biomolecules, Faculty of Chemistry, University of Warsaw,
694 Warsaw 02-093, Poland

695 **Piotr Szustakiewicz** – Laboratory of organic nanomaterials and
696 biomolecules, Faculty of Chemistry, University of Warsaw,
697 Warsaw 02-093, Poland

698 **Christopher Tollan** – Electron-Microscopy Laboratory, CIC
699 nanoGUNE, Basque Research and Technology Alliance
700 (BRTA), Donostia, San Sebastián 20018, Spain

701 **Sanoj Raj** – Department of Chemistry, University of Illinois at
702 Chicago, Chicago, Illinois 60607, United States

703 Complete contact information is available at:

704 <https://pubs.acs.org/10.1021/jacs.0c06446>

705 Author Contributions

706 All authors have given approval to the final version of the
707 manuscript.

Notes

The authors declare no competing financial interest.

■ ACKNOWLEDGMENTS

This work was cosupported by the REINFORCE project
(Agreement No. First TEAM2016-2/15) carried out within
the First Team program of the Foundation for Polish Science
cofinanced by the European Union under the European
Regional Development Fund. L.M.L.-M. acknowledges support
from the Maria de Maeztu Units of Excellence Program from
the Spanish State Research Agency, Grant No. MDM-2017-
0720. The work was cosupported by the MOBILITY Plus
programme (Agreement No. 1259/MOB/IV/2015/0) fi-
nanced by the Polish Ministry of Science and Higher
Education.

■ REFERENCES

- (1) Bodelón, G.; Montes-García, V.; López-Puente, V.; Hill, E. H.; Hamon, C.; Sanz-Ortiz, M. N.; Rodal-Cedeira, S.; Costas, C.; Celiksoy, S.; Pérez-Juste, I.; Scarabelli, L.; La Porta, A.; Pérez-Juste, J.; Pastoriza-Santos, I.; Liz-Marzán, L. M. Detection and Imaging of Quorum Sensing in *Pseudomonas Aeruginosa* Biofilm Communities by Surface-Enhanced Resonance Raman Scattering. *Nat. Mater.* **2016**, *15*, 1203–1211.
- (2) Liu, J.; Guo, J.; Meng, G.; Fan, D. Superstructural Raman Nanosensors with Integrated Dual Functions for Ultrasensitive Detection and Tunable Release of Molecules. *Chem. Mater.* **2018**, *30*, 5256–5263.
- (3) Sevenler, D.; Daaboul, G. G.; Ekiz Kanik, F.; Ünlü, N. L.; Ünlü, M. S. Digital Microarrays: Single-Molecule Readout with Interferometric Detection of Plasmonic Nanorod Labels. *ACS Nano* **2018**, *12*, 5880–5887.
- (4) Dickerson, E. B.; Dreaden, E. C.; Huang, X.; El-Sayed, I. H.; Chu, H.; Pushpanketh, S.; McDonald, J. F.; El-Sayed, M. A. Gold Nanorod Assisted Near-Infrared Plasmonic Photothermal Therapy (PPTT) of Squamous Cell Carcinoma in Mice. *Cancer Lett.* **2008**, *269*, 57–66.
- (5) Li, Z.; Huang, P.; Zhang, X.; Lin, J.; Yang, S.; Liu, B.; Gao, F.; Xi, P.; Ren, Q.; Cui, D. RGD-Conjugated Dendrimer-Modified Gold Nanorods for in Vivo Tumor Targeting and Photothermal Therapy. *Mol. Pharmaceutics* **2010**, *7*, 94–104.
- (6) Khalavka, Y.; Becker, J.; Sönnichsen, C. Synthesis of Rod-Shaped Gold Nanorattles with Improved Plasmon Sensitivity and Catalytic Activity. *J. Am. Chem. Soc.* **2009**, *131*, 1871–1875.
- (7) Bai, X.; Gao, Y.; Liu, H. G.; Zheng, L. Synthesis of Amphiphilic Ionic Liquids Terminated Gold Nanorods and Their Superior Catalytic Activity for the Reduction of Nitro Compounds. *J. Phys. Chem. C* **2009**, *113*, 17730–17736.
- (8) Wu, B.; Liu, D.; Mubeen, S.; Chuong, T. T.; Moskovits, M.; Stucky, G. D. Anisotropic Growth of TiO₂ onto Gold Nanorods for Plasmon-Enhanced Hydrogen Production from Water Reduction. *J. Am. Chem. Soc.* **2016**, *138*, 1114–1117.
- (9) Gu, M.; Zhang, Q.; Lamon, S. Nanomaterials for Optical Data Storage. *Nat. Rev. Mater.* **2016**, *1*, 16070.
- (10) Li, P.; Li, Y.; Zhou, Z. K.; Tang, S.; Yu, X. F.; Xiao, S.; Wu, Z.; Xiao, Q.; Zhao, Y.; Wang, H.; Chu, P. K. Evaporative Self-Assembly of Gold Nanorods into Macroscopic 3D Plasmonic Superlattice Arrays. *Adv. Mater.* **2016**, *28*, 2511–2517.
- (11) Hou, S.; Wen, T.; Zhang, H.; Liu, W.; Hu, X.; Wang, R.; Hu, Z.; Wu, X. Fabrication of Chiral Plasmonic Oligomers Using Cysteine-Modified Gold Nanorods as Monomers. *Nano Res.* **2014**, *7*, 1699–1705.
- (12) Hamon, C.; Novikov, S.; Scarabelli, L.; Basabe-Desmonts, L.; Liz-Marzán, L. M. Hierarchical Self-Assembly of Gold Nanoparticles into Patterned Plasmonic Nanostructures. *ACS Nano* **2014**, *8*, 10694–10703.

- 772 (13) Evans, J. E.; Jungjohann, K. L.; Browning, N. D.; Arslan, I.
773 Controlled Growth of Nanoparticles from Solution with in Situ
774 Liquid Transmission Electron Microscopy. *Nano Lett.* **2011**, *11*,
775 2809–2813.
- 776 (14) Ahmad, N.; Wang, G.; Nelayah, J.; Ricolleau, C.; Alloyeau, D.
777 Exploring the Formation of Symmetric Gold Nanostars by Liquid-Cell
778 Transmission Electron Microscopy. *Nano Lett.* **2017**, *17*, 4194–4201.
- 779 (15) Zhang, D.; Jin, C.; Tian, H.; Xiong, Y.; Zhang, H.; Qiao, P.;
780 Fan, J.; Zhang, Z.; Li, Z. Y.; Li, J. An: In Situ TEM Study of the
781 Surface Oxidation of Palladium Nanocrystals Assisted by Electron
782 Irradiation. *Nanoscale* **2017**, *9*, 6327–6333.
- 783 (16) Vadai, M.; Angell, D. K.; Hayee, F.; Sytwu, K.; Dionne, J. A. In-
784 Situ Observation of Plasmon-Controlled Photocatalytic Dehydrogenation
785 of Individual Palladium Nanoparticles. *Nat. Commun.* **2018**, *9*,
786 4658.
- 787 (17) Tan, S. F.; Raj, S.; Bisht, G.; Annadata, H. V.; Nijhuis, C. A.;
788 Král, P.; Mirsaidov, U. Nanoparticle Interactions Guided by Shape-
789 Dependent Hydrophobic Forces. *Adv. Mater.* **2018**, *30*, 1707077.
- 790 (18) Woehl, T. J.; Prozorov, T. The Mechanisms for Nanoparticle
791 Surface Diffusion and Chain Self-Assembly Determined from Real-
792 Time Nanoscale Kinetics in Liquid. *J. Phys. Chem. C* **2015**, *119*,
793 21261–21269.
- 794 (19) Liu, Y.; Lin, X. M.; Sun, Y.; Rajh, T. In Situ Visualization of
795 Self-Assembly of Charged Gold Nanoparticles. *J. Am. Chem. Soc.*
796 **2013**, *135*, 3764–3767.
- 797 (20) Thorkelsson, K.; Bai, P.; Xu, T. Self-Assembly and Applications
798 of Anisotropic Nanomaterials: A Review. *Nano Today* **2015**, *10*, 48–
799 66.
- 800 (21) Kim, J.; Song, X.; Ji, F.; Luo, B.; Ice, N. F.; Liu, Q.; Zhang, Q.;
801 Chen, Q. Polymorphic Assembly from Beveled Gold Triangular
802 Nanoprisms. *Nano Lett.* **2017**, *17*, 3270.
- 803 (22) Wei, W.; Bai, F.; Fan, H. Oriented Gold Nanorod Arrays: Self-
804 Assembly and Optoelectronic Applications. *Angew. Chem., Int. Ed.*
805 **2019**, *58*, 11956–11966.
- 806 (23) Sutter, E.; Sutter, P.; Tkachenko, A. V.; Krahne, R.; de Graaf, J.;
807 Arciniegas, M.; Manna, L. In Situ Microscopy of the Self-Assembly of
808 Branched Nanocrystals in Solution. *Nat. Commun.* **2016**, *7*, 11213.
- 809 (24) Kim, J.; Ou, Z.; Jones, M. R.; Song, X.; Chen, Q. Imaging the
810 Polymerization of Multivalent Nanoparticles in Solution. *Nat.*
811 *Commun.* **2017**, *8*, 761.
- 812 (25) Ou, Z.; Wang, Z.; Luo, B.; Luijten, E.; Chen, Q. Kinetic
813 Pathways of Crystallization at the Nanoscale. *Nat. Mater.* **2020**, *19*,
814 450–455.
- 815 (26) Chen, Q.; Cho, H.; Manthiram, K.; Yoshida, M.; Ye, X.;
816 Alivisatos, A. P. Interaction Potentials of Anisotropic Nanocrystals
817 from the Trajectory Sampling of Particle Motion Using in Situ Liquid
818 Phase Transmission Electron Microscopy. *ACS Cent. Sci.* **2015**, *1*, 33–
819 39.
- 820 (27) Tan, S. F.; Anand, U.; Mirsaidov, U. Interactions and
821 Attachment Pathways between Functionalized Gold Nanorods. *ACS*
822 *Nano* **2017**, *11*, 1633–1640.
- 823 (28) Novotný, F.; Wandrol, P.; Proška, J.; Šlouf, M. In Situ
824 WetSTEM Observation of Gold Nanorod Self-Assembly Dynamics in
825 a Drying Colloidal Droplet. *Microsc. Microanal.* **2014**, *20*, 385–393.
- 826 (29) Liu, M.; Guyot-Sionnest, P. Mechanism of Silver(I)-Assisted
827 Growth of Gold Nanorods and Bipyramids. *J. Phys. Chem. B* **2005**,
828 *109*, 22192–22200.
- 829 (30) Gómez-Graña, S.; Hubert, F.; Testard, F.; Guerrero-Martínez,
830 A.; Grillo, I.; Liz-Marzán, L. M.; Spalla, O. Surfactant (Bi)Layers on
831 Gold Nanorods. *Langmuir* **2012**, *28*, 1453–1459.
- 832 (31) Alvarez-Puebla, R. A.; Agarwal, A.; Manna, P.; Khanal, B. P.;
833 Aldeanueva-Potel, P.; Carbó-Argibay, E.; Pazos-Pérez, N.; Vigderman,
834 L.; Zubarev, E. R.; Kotov, N. A.; Liz-Marzán, L. M. Gold Nanorods
835 3D-Supercrystals as Surface Enhanced Raman Scattering Spectroscopy
836 Substrates for the Rapid Detection of Scrambled Prions. *Proc. Natl.*
837 *Acad. Sci. U. S. A.* **2011**, *108*, 8157–8161.
- 838 (32) Hamon, C.; Postic, M.; Mazari, E.; Bizien, T.; Dupuis, C.;
839 Even-Hernandez, P.; Jimenez, A.; Courbin, L.; Gosse, C.; Artzner, F.;
840 Marchi-Artzner, V. Three-Dimensional Self-Assembling of Gold
Nanorods with Controlled Macroscopic Shape and Local Smectic B
Order. *ACS Nano* **2012**, *6*, 4137–4146.
- (33) Xie, Y.; Guo, S.; Ji, Y.; Guo, C.; Liu, X.; Chen, Z.; Wu, X.; Liu,
Q. Self-Assembly of Gold Nanorods into Symmetric Superlattices
Directed by OH-Terminated Hexa(Ethylene Glycol) Alkanethiol.
Langmuir **2011**, *27*, 11394–11400.
- (34) Jain, P. K.; Eustis, S.; El-Sayed, M. A. Plasmon Coupling in
Nanorod Assemblies: Optical Absorption, Discrete Dipole Approx-
imation Simulation, and Exciton-Coupling Model. *J. Phys. Chem. B*
2006, *110*, 18243–18253.
- (35) Tira, C.; Tira, D.; Simon, T.; Astilean, S. Finite-Difference
Time-Domain (FDTD) Design of Gold Nanoparticle Chains with
Specific Surface Plasmon Resonance. *J. Mol. Struct.* **2014**, *1072*, 137–
143.
- (36) Han, B.; Shi, L.; Gao, X.; Guo, J.; Hou, K.; Zheng, Y.; Tang, Z.
Ultra-Stable Silica-Coated Chiral Au-Nanorod Assemblies: Core-Shell
Nanostructures with Enhanced Chiroptical Properties. *Nano Res.*
2016, *9*, 451–457.
- (37) Chinwangso, P.; Lee, H. J.; Jamison, A. C.; Marquez, M. D.;
Park, C. S.; Lee, T. R. Structure, Wettability, and Thermal Stability of
Organic Thin-Films on Gold Generated from the Molecular Self-
Assembly of Unsymmetrical Oligo(Ethylene Glycol) Spiroalkanedi-
thiols. *Langmuir* **2017**, *33*, 1751–1762.
- (38) Cao, H.; Guo, F.; Chen, Z.; Kong, X. Z. Preparation of
Thermoresponsive Polymer Nanogels of Oligo(Ethylene Glycol)
Diacrylate-Methacrylic Acid and Their Property Characterization.
Nanoscale Res. Lett. **2018**, *13*, 209.
- (39) Can, A.; Zhang, Q.; Rudolph, T.; Schacher, F. H.; Gohy, J. F.;
Schubert, U. S.; Hoogenboom, R. Schizophrenic Thermoresponsive
Block Copolymer Micelles Based on LCST and UCST Behavior in
Ethanol-Water Mixtures. *Eur. Polym. J.* **2015**, *69*, 460–471.
- (40) Zorn, S.; Skoda, M. W. A.; Gerlach, A.; Jacobs, R. M. J.;
Schreiber, F. On the Stability of Oligo(Ethylene Glycol) (C11EG
6OMe) SAMs on Gold: Behavior at Elevated Temperature in Contact
with Water. *Langmuir* **2011**, *27*, 2237–2243.
- (41) Kunstmann-Olsen, C.; Belić, D.; Bradley, D. F.; Grzelczak, M.
P.; Brust, M. Humidity-Dependent Reversible Transitions in Gold
Nanoparticle Superlattices. *Chem. Mater.* **2016**, *28*, 2970–2980.
- (42) Kohl, H.; Rose, H.; Schnabl, H. Dose-Rate Effect at Low
Temperatures in FBEM and STEM Due to Object-Heating. *Optik*
(Stuttg). **1981**, *58*, 11–24.
- (43) White, E. R.; Mecklenburg, M.; Shevtski, B.; Singer, S. B.;
Regan, B. C. Charged Nanoparticle Dynamics in Water Induced by
Scanning Transmission Electron Microscopy. *Langmuir* **2012**, *28*,
3695–3698.
- (44) Udayabhaskararao, T.; Altantzis, T.; Houben, L.; Coronado-
Puchau, M.; Langer, J.; Popovitz-Biro, R.; Liz-Marzán, L. M.; Vukovic,
L.; Král, P.; Bals, S.; Klajn, R. Tunable Porous Nanoallotropes
Prepared by Post-Assembly Etching of Binary Nanoparticle Super-
lattices. *Science* **2017**, *358*, 514–518.
- (45) Nitka, T. A.; Král, P.; Vuković, L. Configurations of Nanocubes
Floating and Clustering on Liquid Surfaces. *J. Phys. Chem. Lett.* **2019**,
10, 3592–3597.
- (46) Phillips, J. C.; Braun, R.; Wang, W.; Gumbart, J.; Tajkhorshid,
E.; Villa, E.; Chipot, C.; Skeel, R. D.; Kalé, L.; Schulten, K. Scalable
Molecular Dynamics with NAMD. *J. Comput. Chem.* **2005**, *26*, 1781–
1802.
- (47) Johnson, P. B.; Christy, R. W. Optical Constants for Noble
Metals. *Phys. Rev. B* **1972**, *6*, 4370.
- (48) Wang, M.; Park, C.; Woehl, T. J. Quantifying the Nucleation
and Growth Kinetics of Electron Beam Nanochemistry with Liquid
Cell Scanning Transmission Electron Microscopy. *Chem. Mater.* **2018**,
30, 7727–7736.
- (49) Woehl, T. J.; Abellan, P. Defining the Radiation Chemistry
during Liquid Cell Electron Microscopy to Enable Visualization of
Nanomaterial Growth and Degradation Dynamics. *J. Microsc.* **2017**,
265, 135–147.
- (50) Yu, W.; He, X.; Vanommeslaeghe, K.; MacKerell, A. D. 908
Extension of the CHARMM General Force Field to Sulfonyl- 909

- 910 Containing Compounds and Its Utility in Biomolecular Simulations. *J.*
911 *Comput. Chem.* **2012**, *33*, 2451–2468.
- 912 (51) Allouche, A. Software News and Updates Gabedit — A
913 Graphical User Interface for Computational Chemistry Softwares. *J.*
914 *Comput. Chem.* **2011**, *32*, 174–182.
- 915 (52) Darden, T.; York, D.; Pedersen, L. Particle Mesh Ewald: An N·
916 log(N) Method for Ewald Sums in Large Systems. *J. Chem. Phys.*
917 **1993**, *98*, 10089–10092.
- 918 (53) Homeyer, N.; Gohlke, H. Free Energy Calculations by the
919 Molecular Mechanics Poisson-Boltzmann Surface Area Method. *Mol.*
920 *Inf.* **2012**, *31*, 114–122.
- 921 (54) Vergara-Jaque, A.; Comer, J.; Monsalve, L.; González-Nilo, F.
922 D.; Sandoval, C. Computationally efficient methodology for atomic-
923 level characterization of dendrimer-drug complexes: A comparison of
924 amine- and acetyl-terminated PAMAM. *J. Phys. Chem. B* **2013**, *117*,
925 6801–6813.
- 926 (55) Tanner, D. E.; Chan, K. Y.; Phillips, J. C.; Schulten, K. Parallel
927 Generalized Born Implicit Solvent Calculations with NAMD. *J. Chem.*
928 *Theory Comput.* **2011**, *7*, 3635–3642.